# An Efficient Parametrized Optical Infrared Thermography 3D Finite Element Framework for Computer Vision Applications

Zongfei Tong[1,2], Saeid Hedayatrasa[1], Liangliang Cheng[1], Cuixiang Pei[2], Zhenmao Chen[2], Shejuan Xie[2*], Mathias Kersemans[1*]

[1]Mechanics of Materials and Structures (UGent-MMS), Department of Materials, Textiles and Chemical Engineering (MaTCh), Ghent University, 9052 Zwijnaarde, Belgium

[2]State Key Laboratory for Strength and Vibration of Mechanical Structures, Shaanxi Engineering Research Center of Nondestructive Testing and Structural Integrity Evaluation, Xi'an Jiaotong University, 710049 Xi'an, China

**Matching infrared thermography (IRT) with deep learning-based computer vision has recently gained a lot of interest for automated defect assessment in materials. One of the remaining bottlenecks concerns the necessity of a large and diverse experimental and/or virtual training dataset in order to achieve a sufficiently generalizable computer vision algorithm. This paper presents a parametrized 3D finite element (FE) framework, implemented in Fortran90, for efficiently simulating optical infrared thermographic inspection of multi-layer anisotropic media and establishing large-scale virtual dataset with sufficient diversity. The interface element is introduced for the modelling of an imperfect thermal contact, allowing to simulate a variety of defect types. The flexibility**

**of the interface element makes it possible to simulate delaminations with different thickness using the same discretized model. Validation is done for two benchmark cases which are representative for a fiber reinforced polymer laminate with delamination-like defects. In order to achieve true-to-nature thermographic simulation data, non-uniform heating conditions are adopted from experiment, and a stochastic morphology generator is introduced for modelling realistic irregular defect geometries. To demonstrate the added value of a large, diverse and true-to-nature virtual database for computer vision applications, a Faster-RCNN model was trained on a generated virtual dataset for the detection of delamination-like defects in fiber reinforced polymer laminates. Application of the trained Faster-RCNN on experimental thermographic data yields excellent inference results, illustrating the high generalization ability of the virtually trained object detector.**

***Index Terms*—infrared thermography, carbon fiber reinforced polymer, finite element method, interface element, computer vision, virtual dataset**

# 1. INTRODUCTION

Fiber reinforced polymer (FRP) composites, such as glass fiber reinforced polymers (GFRPs) and carbon fiber reinforced polymers (CFRPs), have become an important material for many industry applications due to their high performance, e.g. high strength-to-weight ratio and corrosion resistance [1]. One of the major drawbacks of composite materials is their susceptibility to damage features, like foreign material inserts, (matrix)cracks, delaminations and impact damage. These defects may initially be very small and insignificant, but they can significantly grow over time leading to a severe degradation of the component's structural performance [2]. Therefore, non-destructive testing (NDT) techniques are needed to detect defects as early as possible, and as such to assure the structural safety and long-term reliability of FRP components [3].

A diversity of NDT techniques for inspection of FRP are available in literature, including visual inspection [4], ultrasonic testing [5], vibrational testing [6] and infrared thermography [7, 8]. Among these techniques, optical infrared thermography (IRT) is an attractive method as it enables remote and full-field detection of defects. The thermal contrast between defective and non-defective regions is normally weak and potentially degraded by uneven distribution of heat, noise sources, environmental reflections, and variability in the emissivity of the target surface. Therefore, a range of postprocessing algorithms, such as principal component thermography (PCT) [9], thermal signal reconstruction (TSR) [10], and pulsed phase thermography (PPT) [11, 12], have been proposed to counteract these factors, and as such to improve the defect detectability in thermographic inspection[13, 14].

The rapid developing of deep learning-based computer vision(CV) algorithms shows a significant potential to detect defects automatically from thermographic images and to bring the IRT technique to the next level [15-18]. Specifically, CV algorithms can play important roles in automatic defect classification, defect identification, and defect segmentation using IRT image sequences. The object detection algorithms, like Faster R-CNN [19] and YOLOv3 [20], can be employed to determine the types, positions, and rough sizes of the defects, while the image segmentation algorithms, such as U-Net [21] and DeepLabv3 [22], are valuable to segment the exact shapes of the defects. A crucial part in the performance and generalization of a supervised CV algorithms is the availability of a large and diverse set of thermographic images covering the variability in inspection conditions as much as possible. Setting up a sufficiently large and diverse experimental training database is difficult to achieve in practice, although there have been some recent initiatives taken [23]. In order to boost the application of CV algorithms in the IRT field, the use of numerical models is a reasonable alternative. In this regard, several developments have been introduced so far in literature. Finite element method(FEM) [24], Finite volume method(FVM) [25], and semi-analytical method [26] have been investigated to simulate the thermal response of a delamination in FRP. In the field of FEM applied in thermography, most of the works use volume elements with different thermal properties to model a defect. Reference [27] investigated thermal responses of different configurations, such as various depth, size, and defect nature. Using FEM and iterative inverse procedure, the authors from reference [28] reconstruct ply orientation in thin CFRP laminates using eddy current thermography. Reference [29] adjusted a series of numerical parameters to obtain simulation results as close as possible to those obtained experimentally. Reference [30] implemented the multi-medium element to simulate delamination defects in

metallic structures. Although these numerical methods show good accuracy in simulating the thermal response from a delamination defect, they lack computational efficiency for generating a realistic database. This is understood considering that delamination thickness varies in reality, with typical delamination thickness values below 15 μm [31]. As the thickness of a delamination defect is much smaller than the typical ply thickness in FRP laminates, the use of volume elements is not straightforward from geometrical point of view.

As an alternative, several authors employed the discontinued nodes(DN) method to model delaminations [24]. Compared with the volume element method, the DN method considerably reduces the number of elements and as such is computationally far more efficient. However, as a result of completely inhibiting thermal diffusion between the interfaces of the modeled delamination, the DN method produces a rather unrealistic thermal response for delamination defects. This approach actually over estimates the thermal contrast induced by the defect and provides results which are closer to the thermal response of flat bottom hole defects [32]. Another alternative could be the use of interface elements to represent an imperfect contact [33]. Reference [34] utilized linear interface elements to simulate the temperature and stress distributions of orthotropic layered slabs. Their results showed that the interface element can model an imperfect (thermal) contact in a proper manner. Reference [35] used interface elements to model an oxide film in heat transfer analysis. Interface elements were employed to capture displacement jumps and proposed several interface constitutive laws [36]. Reference [37] applied interface elements to simulate the mechanical responses of delaminations in FRP. These classic studies indicate that the interface element can efficiently simulate imperfect contacts with different thicknesses in a geometrically reasonable way.

For CV applications it is crucial that the numerical framework can cope with the wide range of experimental parameters in order to populate a sufficiently large and diverse virtual database. There should be diversity in the way of optical excitation in order to cope with the typical non-uniform heating profiles encountered in experiments [38]. Additionally, many studies in literature consider simple geometric shapes for delamination defects (e.g. circular, elliptic or rectangular) [16, 26], while real defects rarely have such a simplified shape. Therefore, it is crucial for CV algorithms that the training database contains sufficiently diverse defect geometries which are a good representation of irregular defect morphologies found in reality. Obviously, the training database should also have sufficient diversity in the size and depth of defects in order to increase the performance of a CV algorithm. Also delamination thicknesses should be taken as an explicit variable. It may be clear that existing (commercial) FE software modules have difficulty (and even limitations) to cope with the above factors for guaranteeing both computational efficiency and diversity of simulations.

In this study, the authors present a parametric FEM methodology, programmed in Fortran90, in order to generate a realistic, large and diverse virtual thermographic database for CV applications. The developed framework can handle heat transfer in multi-layer anisotropic structures, such as FRP materials. Interface elements have been implemented to model the heat transfer at imperfect thermal interfaces, and as such to simulate the thermal response of delamination-like defects in a geometrically reasonable manner. To achieve sufficiently diverse simulation data for deep learning applications, randomly positioned non-uniform optical excitation has been implemented by adapting experimental conditions. Furthermore, a random morphology strategy is introduced which enables modelling of

realistic defects with irregular shapes. A virtual dataset is established using proposed method. Faster-RCNN trained on the virtual dataset was tested on the experimental results.

The structure of this paper is organized as follows. The FEM formulation of heat transfer and the interface element is introduced in section 2. Section 3 validates the reliability of the implemented FE framework with a commercial software package for two benchmark cases. Section 4 introduces the stochastic parametrization of the FE framework to achieve non-uniform heat generation conditions as well as to generate realistic defect morphologies. A large and diverse virtual dataset, generated by the proposed parametrized FE framework, was used for training a Faster-RCNN in section 5. The trained Faster-RCNN is then applied on experimental data from FRP laminates with delamination-like defects. The conclusions are reported in section 6.

## 2. FORMULATION OF PROPOSED NUMERICAL METHOD

Optical thermography involves the absorption of the radiation of an optical source, resulting in the generation of heat at the surface of the inspected sample, followed by heat conduction inside the sample, and thermal convection and radiation between the sample's surface and environment. A schematic of the numerical model, together with the relevant coordinate system, is provided in Fig.1.

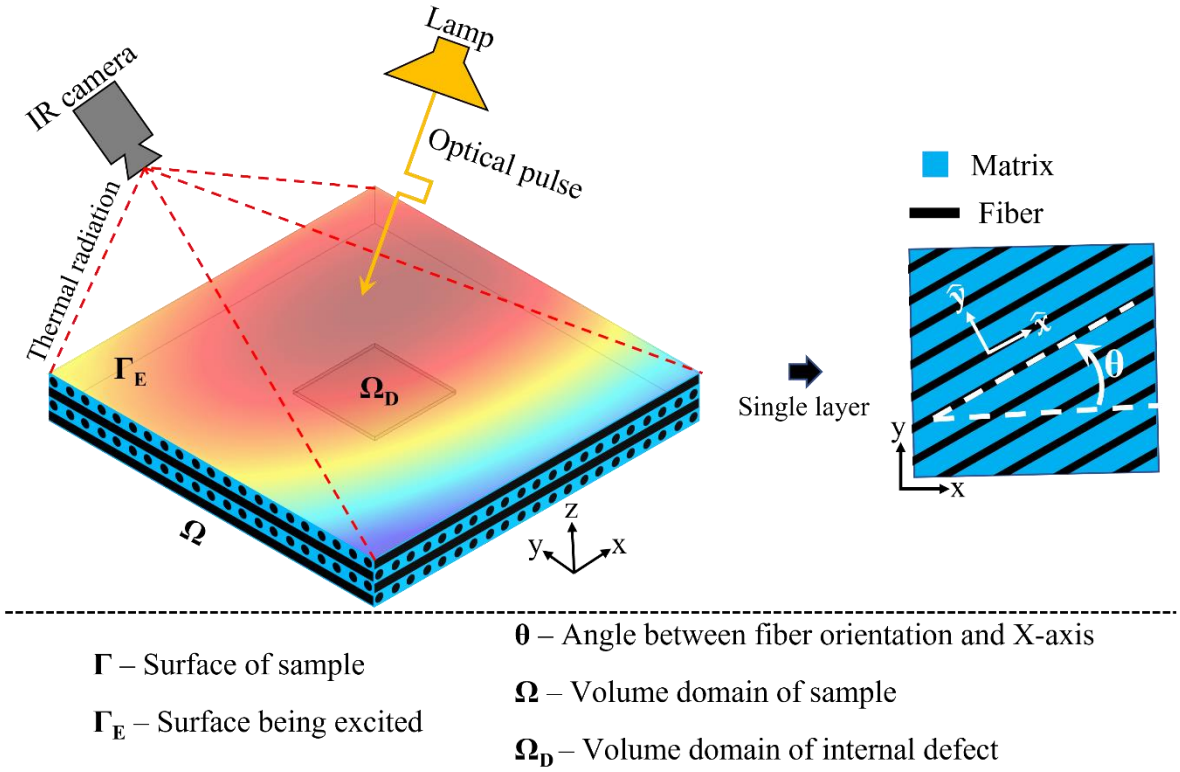


Figure 1 Schematic of optical thermography and definition of different volume domains and surface regions.

## 2.1. Optical radiation

The radiation from an optical source, which is absorbed by the surface of the inspected sample, can be interpreted as a thermal flux which is directly subjected to the inspected surface. This approach is computationally efficient, but it needs a proper way to define a realistic distribution of this thermal flux. The thermal flux on the surface of the sample, stimulated by an optical lamp, can be generally expressed as,

$$q_{flux} = q(x, y, t) = (q_{max} e) \cdot f(t) \cdot g(x, y) \quad (1)$$

where $q_{max}$ [W/m$^2$] denotes the amplitude of heat flux, $e$ [-] is the emissivity of the sample's surface, $f(t)$ represents the waveform of the excitation signal, and $g(x, y)$ describes the

spatial radiation distribution of the optical lamp at a certain distance. In case of a spatially uniform heating profile, $g(x,y)$ is identical to 1.

The thermal flux on the sample's surface produced by an optical lamp can be regarded as a Neuman boundary condition in the thermal analysis. The Neuman boundary condition can be expressed as[39],

$$-\bar{\bar{k}}\frac{\partial T}{\partial n} = q_{flux} \quad \text{on } \Gamma_E \tag{2}$$

Where $T$ [K] represents temperature, $n$ denotes the coordinate axis in the direction of the unit normal vector $\boldsymbol{n}$, $q_{flux}$ [W/m$^2$] denotes the thermal flux applied on the boundary $\Gamma_E$ of the sample, $\bar{\bar{k}}$ [W/(m·K)] denotes the anisotropic body thermal conductivity matrix which has the form,

$$\bar{\bar{k}} = \begin{bmatrix} k_{xx} & k_{xy} & 0 \\ k_{yx} & k_{yy} & 0 \\ 0 & 0 & k_{zz} \end{bmatrix} \tag{3}$$

$$k_{xx} = k_{\hat{x}}\cos^2(\theta) + k_{\hat{y}}\sin^2(\theta) \tag{4}$$

$$k_{xy} = k_{yx} = \frac{k_{\hat{x}} - k_{\hat{y}}}{2}\sin(2\theta) \tag{5}$$

$$k_{yy} = k_{\hat{x}}\sin^2(\theta) + k_{\hat{y}}\cos^2(\theta) \tag{6}$$

$$k_{zz} = k_{\hat{z}} \tag{7}$$

where $k_{\hat{x}}$, $k_{\hat{y}}$, and $k_{\hat{z}}$ are the thermal conductivities of a FRP ply along the fibers, and transverse to the fibers. $\theta$ is the angle between the fiber orientation in a ply and the X-axis, and as such represents the ply angle in the global frame of reference (see Fig. 1).

## 2.2. Heat conduction

Considering energy conservation and Fourier heat conduction, the governing heat equation can be expressed as[39],

$$\rho c \frac{\partial T}{\partial t} = \nabla \cdot \left(\bar{\bar{k}} \nabla T\right) + Q, \quad \text{in } \Omega \tag{8}$$

where $\rho$ [kg/m$^3$], and $c$ [J/(kg·K)] are the density and the specific heat, respectively. $Q$ denotes the rate of heat generated per unit volume, while $\Omega$ represents the domain which needs to be solved.

## 2.3. Thermal convection

Considering the air flow around the inspected sample, the thermal exchange through natural convection between the sample's surface and the surrounding air is implemented by the Robin boundary condition which can be presented as,

$$-\bar{\bar{k}} \frac{\partial T}{\partial n} = h\left(T - T_f\right) \quad \text{on } \Gamma \tag{9}$$

where $h$ [W/(m$^2$·K)] indicates the convection coefficient, $T_f$ represents ambient temperature and $\Gamma$ denotes the surface at which the Robin boundary condition applies.

## 2.4. Spatial discretization

According to the standard FEM procedure, the continuous variable $T$ can be approximated by $\tilde{T}$ in terms of its degree of freedoms (DOFs) of nodes through shape functions (10),

$$\tilde{T} = \{N_l\}\{T_l\}, \quad l = 1,2,\cdots,n \tag{10}$$

where $T_l$ denotes the temperature at the $l^{th}$ node. $N_l$ is the shape function, which is for convenience represented by $N$ in the subsequent analysis. The brackets $\{\cdot\}$ indicate that the variable is a vector.

By means of the continuous Galerkin's method[39] and substituting Eq. (10) into Eq. (8), the discretized formulation of thermal analysis can be expressed as,

$$\bar{\bar{k}}\int_{\Omega}(\nabla\{N\})^{\mathrm{T}}\nabla\{N\}\,\mathrm{d}V\{T\}+\rho c\int_{\Omega}\{N\}^{T}\{N\}\,\mathrm{d}V\left\{\frac{\partial T}{\partial t}\right\}+h\int_{\Gamma_2}\{N\}^{T}\{N\}\,\mathrm{d}S\{T\}=$$

$$\int_{\Omega}\{N\}^{T}Q\,\mathrm{d}V+h\int_{\Gamma_2}\{N\}^{T}T_f\,\mathrm{d}S-\int_{\Gamma_1}\{N\}^{T}q_{flux}\,\mathrm{d}S \tag{11}$$

Considering there is no volume thermal source involved in optical IRT, i.e., $Q$=0, Eq. (11) can be assembled in the whole solution domain and organized in matrix form as,

$$[K]\{T\}+[C]\left\{\frac{\partial T}{\partial t}\right\}=\{F\} \tag{12}$$

where the global conductivity matrix $[K]$, global capacitance matrix $[C]$, and global load vector $[F]$ can be presented as,

$$[K]=\sum\left(\bar{\bar{k}}\int_{\Omega}(\nabla\{N\})^{\mathrm{T}}\nabla\{N\}\,\mathrm{d}V+h\int_{\Gamma_2}\{N\}^{T}\{N\}\,\mathrm{d}S\right) \tag{13}$$

$$[C]=\sum\left(\rho c\int_{\Omega}\{N\}^{T}\{N\}\,\mathrm{d}V\right) \tag{14}$$

$$\{F\}=\sum\left(h\int_{\Gamma_2}\{N\}^{T}T_f\,\mathrm{d}S-\int_{\Gamma_1}\{N\}^{T}q_{flux}\,\mathrm{d}S\right) \tag{15}$$

### 2.5. Incorporating interface elements

If there is an imperfect thermal contact, e.g. delamination defect, the relevant interface conditions can be expressed as,

$$k^{i-1}\frac{\partial T^{i-1}}{\partial z}=k^{i}\frac{\partial T^{i}}{\partial z} \tag{16}$$

$$k^{i-1}\frac{\partial T^{i-1}}{\partial z}=\frac{1}{R^{i}}\left(T^{i}-T^{i-1}\right) \tag{17}$$

where the imperfect thermal contact is supposed to be located between layers $i-1$ and $i$. Eq. (16) guarantees the continuity of the thermal flux at the interface. Eq. (17) states that the difference between the temperatures at the two surfaces of the interface is proportional to the thermal flux through the interface, with the constant of proportionality being the thermal contact resistance $R^i$ [26]. The imperfect thermal contact functional, $\Pi_{interface}$, corresponding to Eq. (16) and (17) can be written as[34],

$$\Pi_{interface} = \sum_{i=1}^{m} \int_0^{L^i} \frac{1}{2} \frac{L^i}{R^i} (\nabla T)^2 \, \mathrm{d}V \tag{18}$$

where $m$ is the number of imperfect thermal contacts, $L^i$ is the thickness of the $i^{th}$ imperfect thermal contact which geometrically approaches zero.

The hexahedron element with eight nodes and linear shape function is adopted both for the volume elements and interface elements. Substituting the hexahedron element into the stationary functional of Eq. (18) leads to the matrix representation,

$$[K_I]\{T\} = \{0\} \tag{19}$$

where $[K_I]$ is the global conductivity interface matrix, which can be derived from Eq. (18) according to the variational approach and represented as,

$$[K_I] = \sum_{j=1}^{n_I} \int_{\Omega_D} \frac{L_j}{R_j} (\nabla N)^T \nabla N \, \mathrm{d}V \tag{20}$$

where $L_j$ the thickness and thermal contact resistance of $j^{th}$ interface element, $n_I$ is the number of interface elements, $\Omega_D$ represents the delamination region, $R_j$ is the thermal contact resistance of $j^{th}$ interface element, which has the form,

$$R_j = \frac{L_j}{k_d} \tag{21}$$

where $k_d$ is the thermal conductivity of the imperfect thermal contact.

Finally, combining Eq. (12) and (19), the discretized formulation of optical thermography for multi-layer anisotropic media, incorporating imperfect thermal contacts to represent embedded defects, can be written as,

$$([K]+[K_I])\{T\}+[C]\left\{\frac{\partial \mathrm{T}}{\partial \mathrm{t}}\right\}=\{F\} \tag{22}$$

### 2.6. Temporal discretization

The Crank-Nicolson (CN) strategy is employed to conduct temporal discretization of Eq. (22), which can be given as [39],

$$\frac{\partial T(t)}{\partial t}+\frac{\partial T(t-\Delta t)}{\partial t}\approx 2\frac{\left(T(t)-T(t-\Delta t)\right)}{\partial t} \tag{23}$$

Substituting Eq. (23) into Eq. (22) gives,

$$([K]+[K_I])T(t)+[C]\left\{2\frac{\left(T(t)-T(t-\Delta t)\right)}{\partial t}-\frac{\partial T(t-\Delta t)}{\partial t}\right\}=\{F(t)\} \tag{24}$$

Considering,

$$([K]+[K_I])\{T(t-\Delta t)\}+[C]\left\{\frac{\partial T(t-\Delta t)}{\partial t}\right\}=\{F(t-\Delta t)\} \tag{25}$$

The final temporal discretization formulation of Eq. (22) can be expressed as,

$$\left([K]+[K_I]+\frac{2[C]}{\Delta t}\right)\{T(t)\}=\{F(t)+F(t-\Delta t)\}+\left(\frac{2[C]}{\Delta t}-[K]-[K_I]\right)\{T(t-\Delta t)\} \tag{26}$$

The here presented FE framework has been implemented in Fortran90.

## 3. THE NUMERICAL BENCHMARKS FOR VALIDATION

The implemented FE framework (section 2) is validated and benchmarked with the commercial software package Ansys . Two numerical benchmarks are performed, a simple

model and a more complex model, in order to illustrate the reliability of the presented FE framework.

A delamination-like defect in multi-layer FRP leads to a local discontinuity of the thermal properties, and can be modeled in different ways. In commercial software packages, one could model the delamination with volume elements (VE) and discontinued nodes (DN) method. The presented FE approach in section 2 additionally allows to model a delamination with interface elements (IE). A schematic diagram of the different options to model a delamination-like defect is given in Fig.2.

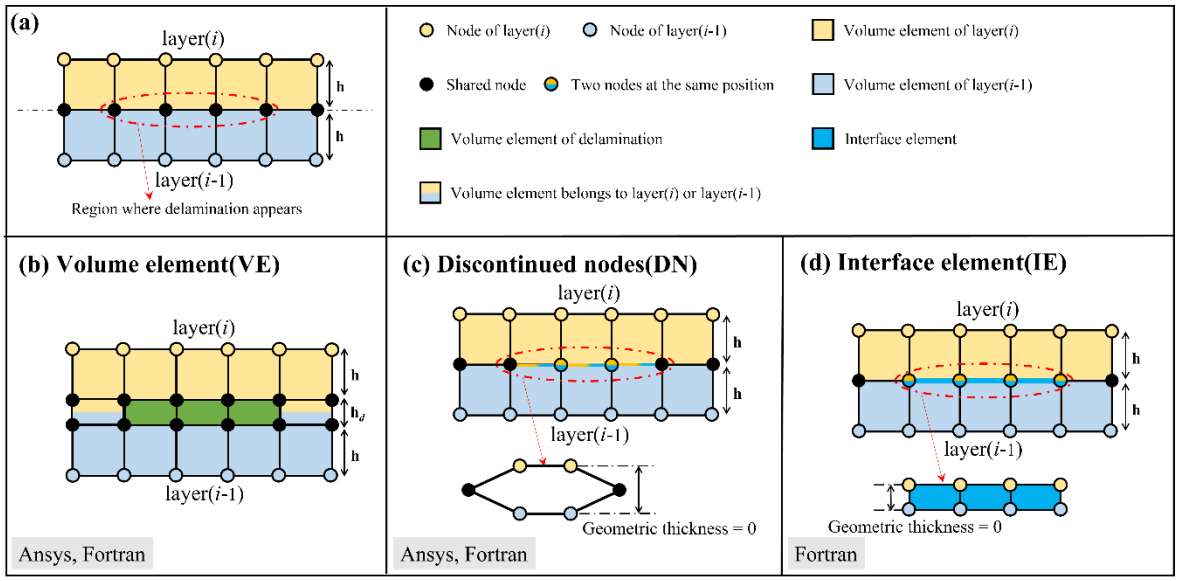


Figure 2 Delamination simulation using FEM with various strategies. (a) Model without delamination. Model with delamination modelled by (b) volume element (VE), (c) discontinued nodes (DN), and (d) interface element (IE).

In the VE method (see Fig. 2(b)), volume elements are added in-between the FRP layers. Fig. 2(c) shows the geometrical details of the DN method. Two nodes, belonging to different layers, are located in the delamination region and do not allow to transfer energy with each other. It may be expected that this hard thermal discontinuity condition will provide a too

simplified view on the thermal response of realistic delamination defects. Finally, the IE method is displayed in Fig. 2(d), which presents the delamination in a physically and geometrically reasonable manner.

### 3.1. Benchmark I: FRP laminate with single delamination

The first numerical benchmark involves a square CFRP sample of size $50 \times 50 \times 0.8$ mm$^3$ and unidirectional stacking sequence $[0_4]$, see Fig. 3. A delamination-like defect of size $10 \times 10$ mm$^2$ is located in the middle of the sample. The delamination is assumed to be a defect with a thermal resistance equivalent to a thin air layer with a thickness of 10 μm (except for the DN method where it has infinite thermal resistance). The employed material properties are listed in Table 1. A uniform heat flux of 5000 W/m$^2$ is applied on the top surface of the sample. The heating stage lasts 10 s, followed by a cooling stage of 10 s. The time increment is set at 0.05 s. The convection boundary condition has a coefficient equal to 5 W/(m$^2$·K). The temperature distribution along the black line at 10 s, and the temperature evolution at the orange point P, are extracted to investigate the spatial and temporal accuracy of the various modelling approaches (see Fig. 4).

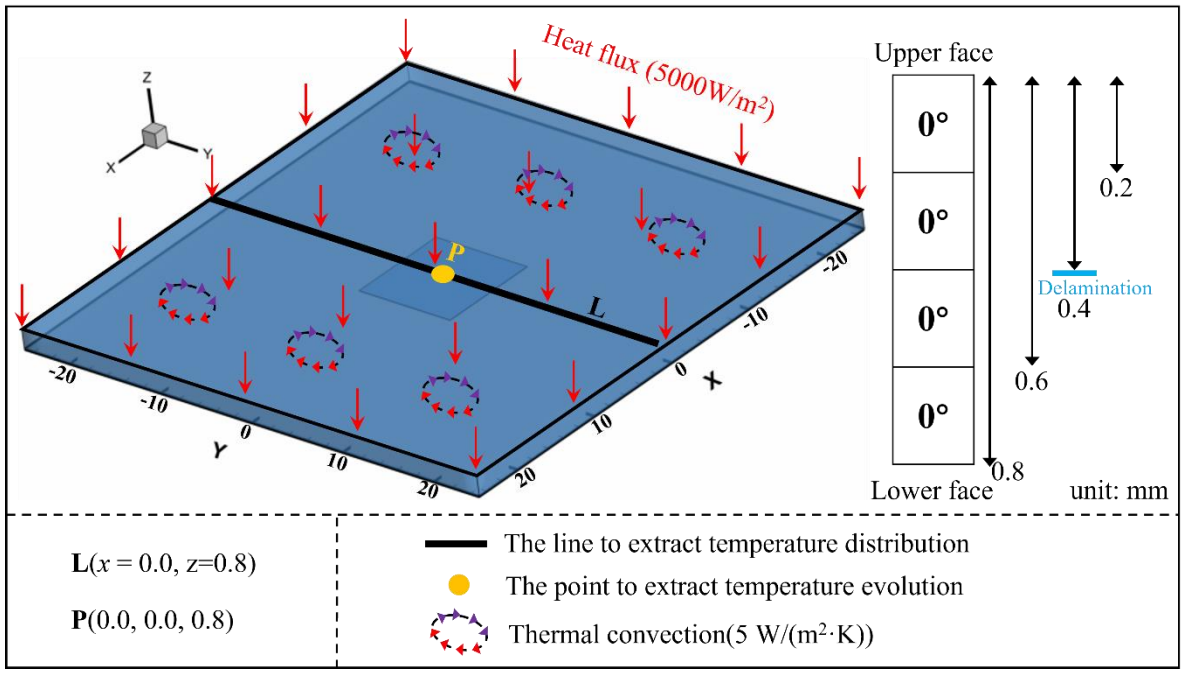


Figure 3 Numerical model of benchmark I

Table 1 Material properties used in benchmark I

| Material properties | Values |
|---|---|
| Density ρ [kg/m$^3$] | 1530 |
| Specific heat c [J/(kg·K)] | 917 |
| Thermal conductivity $\bar{\bar{k}}$ [W/m·K] | $k_x = 2.71, k_y = 0.61, k_z = 0.53$ |
| Thermal conductivity of delamination $k_d$ [W/m·K] | 0.0259 |
| Thickness of delamination L [μm] | 10 |
| Ambient temperature [°C] | 25 |

Figure 4 displays the thermal results obtained along the line segment L (at t = 10 s) and at the point P, for the different modeling approaches. The results for the traditional VE method are presented in Fig. 4(a-b). The results clearly show the good agreement between the solution provided by the commercial solver (Ansys) and our own implemented solver in

Fortran. The relative error over the line segment L (at t = 10s) is in the range of 0.004% - 0.012%, while the relative error of the temperature evolution at point P is mainly below 0.2%. At the onset (t = 0 s) and end (t = 10 s) of the applied surface flux, the relative error at point P shortly increases to values up to ~1%.

The results for the DN method are displayed in Fig. 4(c-d), showing a good agreement between the solution provided by the commercial solver, and the here presented FE framework. The results further indicate that the DN method provides a significantly higher temperature contrast at the delamination region in comparison to the case of volume element method (see Fig. 4(a)). Fig. 4(d) reveals the stronger heating/cooling rate in case of the DN approach. This behavior could have been expected considering that the DN method does not allow any heat transfer through the defect interfaces, and as such leads to increased heat build-up above the defect during the heating phase.

At last, the results obtained with the IE method are presented in Fig. 4(e-f). A good correspondence for both spatial and temporal results is obtained with the VE method. Similar error rates are obtained as in Fig4(a-b). Hence, these results clearly indicate that the implemented interface elements provide a suitable alternative to volume elements for simulating delamination-like defects in FRPs.

Figure 5 provides a qualitative comparison of the computed thermal surface fields at different time instances. In line with the results presented in Figure 4, there is a good visual correspondence between the results obtained with the VE method and the IE method. The temperature maps for the DN method show much higher temperatures, compared to the VE or IE method, at the delamination zone. Especially in the cooling stage (t > 10 s), large discrepancies are found in comparison with the VE (and IE) method. The results for figure 4

and figure 5 clearly indicate that the DN methods are physically unreasonable to simulate the thermal response of a delamination-like defect. Instead, the VE method and IE method are the preferred choice, showing good correspondence to each other.

In order to compare the computational efficiency of the different modelling strategies, they are implemented using the same CPU (Intel i7-10875H) and the computational times are listed in table 2. Overall, it can be observed that the computational times in the Fortran implementation as smaller. Though, it has to mentioned that the computational efficiency of the commercial software Ansys compared to the developed simulator in Fortran should be interpreted with care. On the one hand, it cannot be guaranteed that both implementations are calculated under exactly the same conditions, such as temporal discretization method and convergence conditions. On the other hand, the commercial software Ansys adopts a surface element to apply two boundary conditions, i.e. Equation (2) and (9), on the sample's surface. This introduces additional computational steps which leads to an increased computational time. More interestingly is the comparison between the different modelling approaches within a software package. For Ansys, the computational benefit of using DN method is clearly demonstrated. The computational efficiency of the models with VE, DN and IE is comparable using the developed simulator in Fortran.

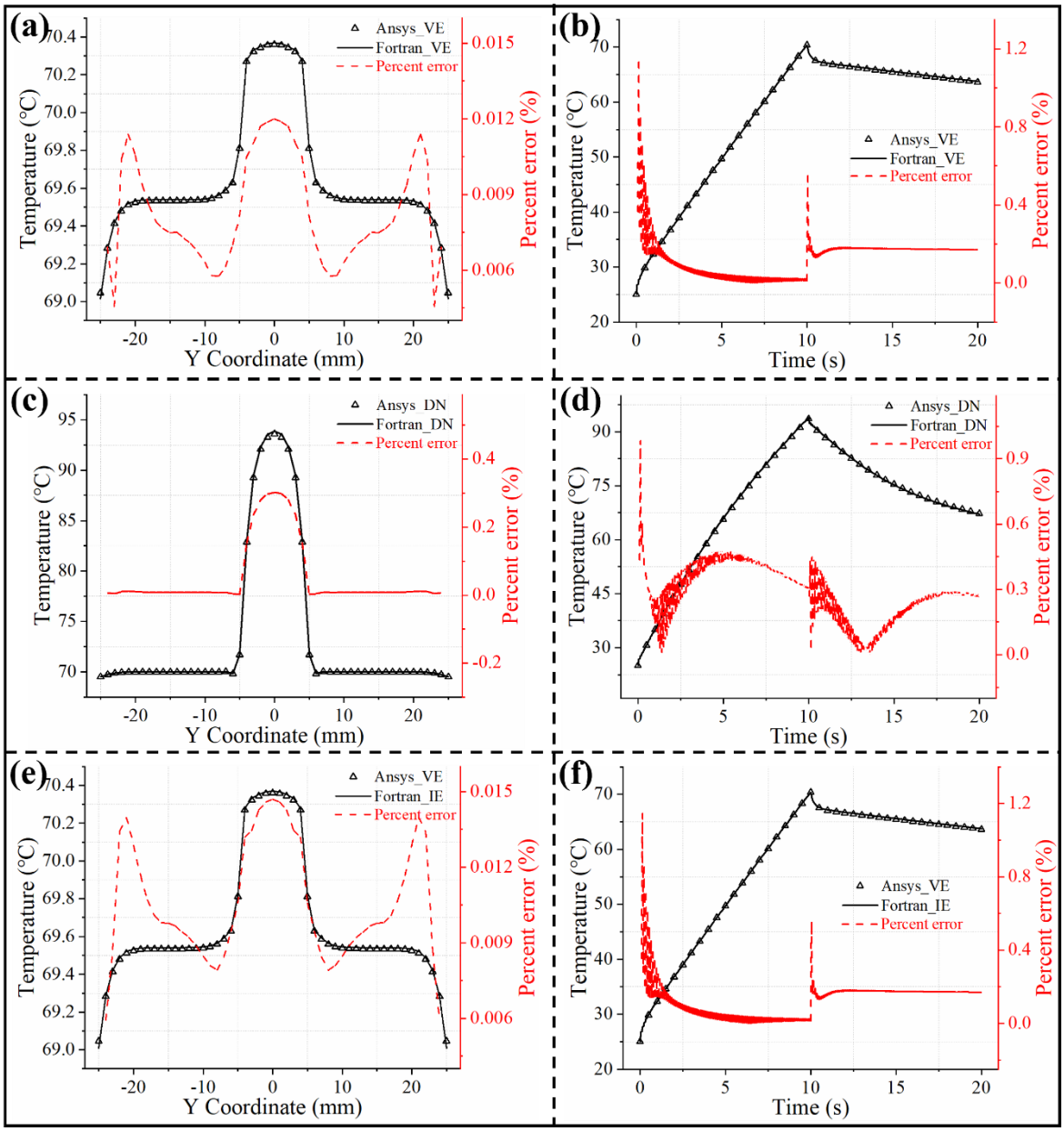


Figure 4 Thermal results of benchmark I comparing different numerical methods: (left) along line segment L at t = 10 s and (right) at point P.

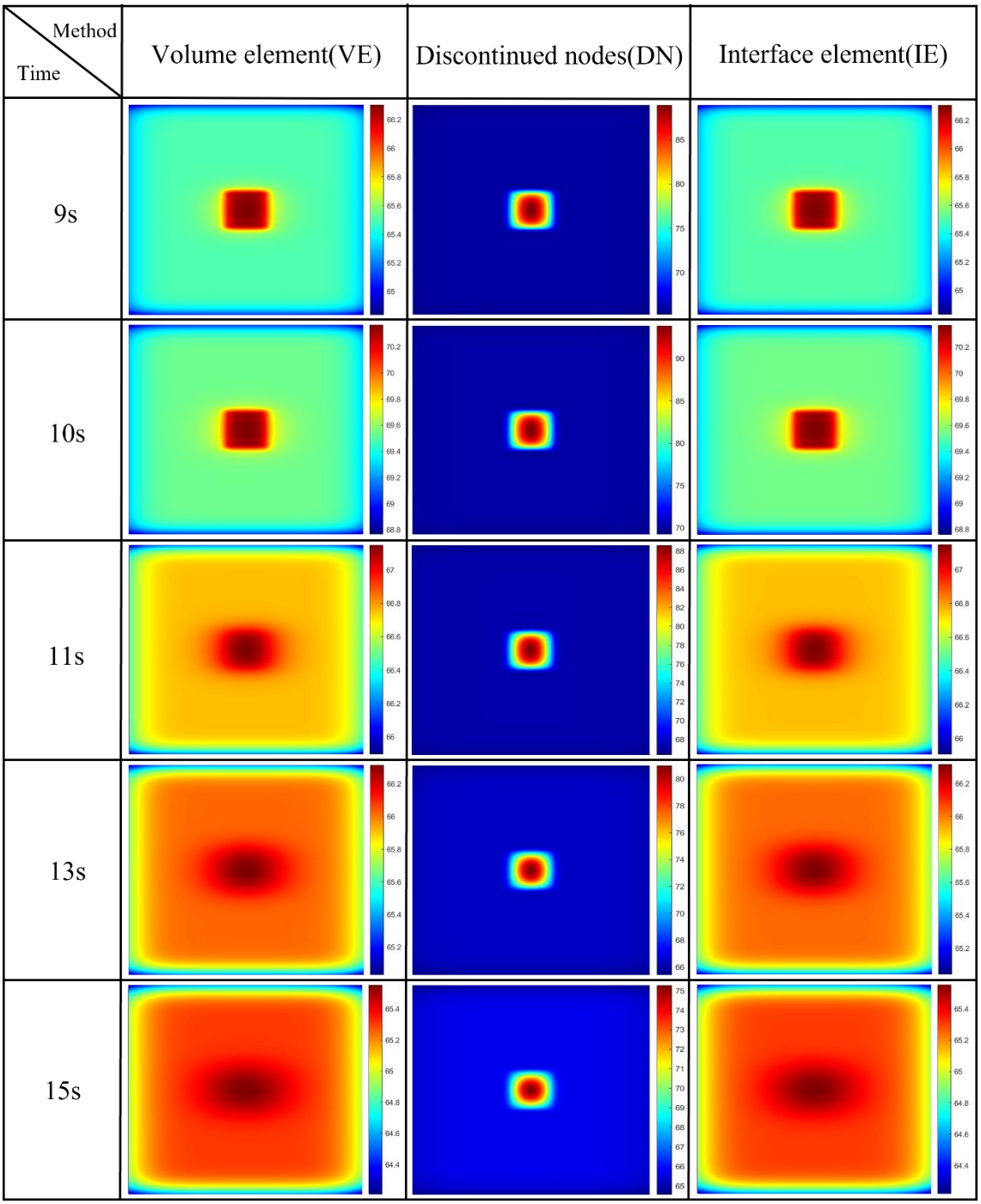


Figure 5 Computed surface temperature at various times for different modelling methods (in Fortran).

Table 2 Simulation efficiency comparison for benchmark I. Computations have been performed using single CPU Intel i7-10875H

| | **VE** | **DN** | **IE** |
|---|---|---|---|
| Number of mesh elements | 27500 | 25000 | 27500 |
| Computational time (Ansys) | 574 s | 498 s | — |
| Computational time (Fortran) | 111 s | 107 s | 112 s |

For the numerical model in Fig. 4, both the VE and IE was inserted at the full interlayer where the delamination is located. This allows to simulate a set of models with arbitrary delamination geometries using a single mesh distribution. The thickness of the VE and IE equals to 10 μm in Fig. 4 for both delamination region and sound region of the interlayer. This is not in correspondence with reality where the thickness of the sound region in this interlayer should approach 0. With the IE approach, it is possible to locally change the thickness without having to change the mesh distribution. To understand the influence of the interlayer thickness in the sound region, numerical models comprising 1~10 μm thickness IE in sound region and 10 μm thickness IE in delamination region (see Fig. 6(a)) were investigated. The results clearly show that the thickness of the sound interlayer has a significant impact of the temperature distribution on the surface (Fig. 6(b)) and over the depth of laminate (cross-section x=0 mm in Fig. 6(c)), at an arbitrary time instance 10 s. As the thickness of sound interlayer increases, the heat is more efficiently laterally dissipated into the surrounding sound material at the defect's plane, and a higher fraction of it is transferred to the remaining thickness below the defect (Fig. 6(c)). As a result, increasing the thickness of the sound interlayer lowers the temperature at both defect region and sound region on the top surface, but increases the defect-induced thermal contrast (Fig. 6(b)). This demonstrates

the added value of interface elements in giving control over the lateral heat dissipation at defect's plane by changing the interlayer sound thickness, while tackling the geometrical inconsistency with defect's thickness.

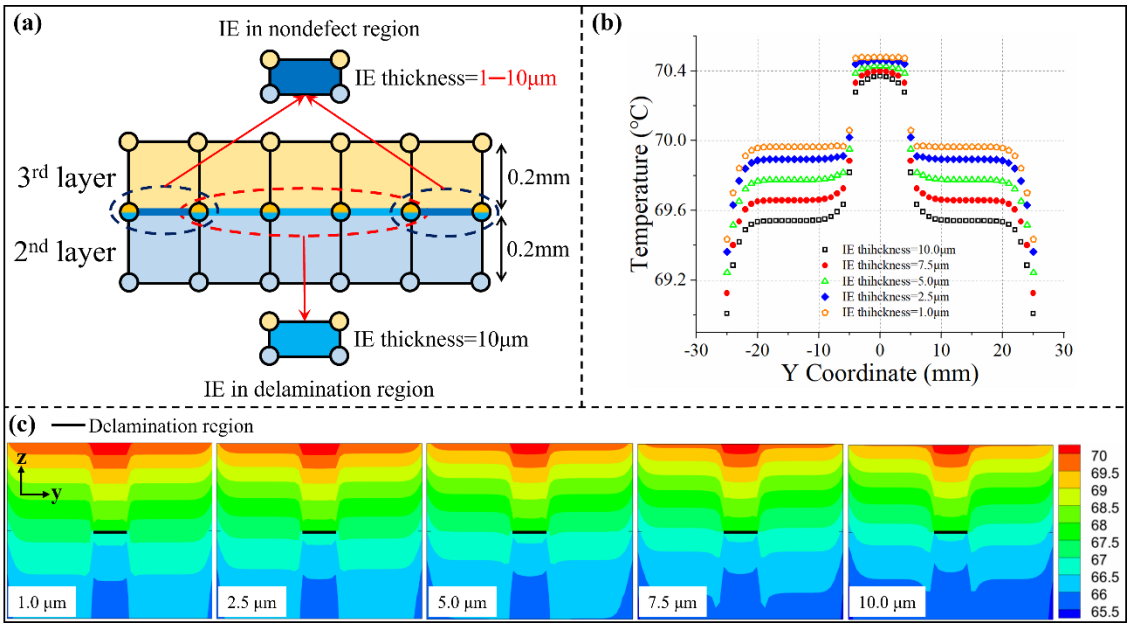


Figure 6 (a) The diagram of the numerical model with various thickness of the IE in sound region, (b) line temperature distribution along line segment L at 10 s (see Figure 3), and (c) the temperature field of the cross-section (x=0 mm) at 10 s.

### 3.2. Benchmark II: FRP laminate with multiple delaminations

In this section, a validation study is done on the accuracy, robustness and of the developed methodology for a more complex model. Figure 7 schematically shows the numerical benchmark II, which consists of a quasi-isotropic $[(0/+45/90/-45)]_S$ CFRP laminate with size $320 \times 90 \times 1.84$ mm$^3$. Seven delaminations with different sizes are located between the layers at different depths. Same as benchmark I, a uniform heat flux with 5000 W/m$^2$ is applied on the top surface of the sample. The excitation parameters and boundary conditions are consistent with benchmark I. Other material properties are the same as those reported in Table

1. From the results of benchmark I, it was clear that the DN method provides unrealistic thermal simulation results. Therefore, the discussion for Benchmark II is limited to the results obtained by the VE and IE method.

Figure 8 displays the temperature distribution along the black line L at 10 s and the temperature evolution at the orange point P (see indicators on Fig. 7). For the VE approach, a good correspondence is obtained between the commercial software Ansys and our Fortran implementation. Along the line L, the relative error between both methods is limited to 0.01%. The relative error on the temperature evolution at point P is mostly within 0.1%. However, similar as in Benchmark I, the error rate shortly increases at the onset and end of the heating stage up to a value of ~1%. The comparative analysis between the VE method and the IE method is presented in Fig. 8(c-d). Both the spatial temperature distribution and temporal temperature evolution of the model adopting IE have a great consistency with VE method, showing the same error rates as in Fig. 8(a-b). Table 3 reports the computation time, using single CPU Intel i7-10875H, to calculate the model in Benchmark II. Hence, these results confirm that the IE method is a valid alternative for the classical VE approach, yielding highly accurate temperature results in a comparable computational efficiency.

In order to illustrate the effect of various thicknesses of the sound region of the interlayer on the computed thermal results, the surface temperature fields at different time instances are shown in Fig. 9. Especially in the cooling-down stage pronounced differences can be observed, revealing the added value of using IE for modelling delamination-like defects.

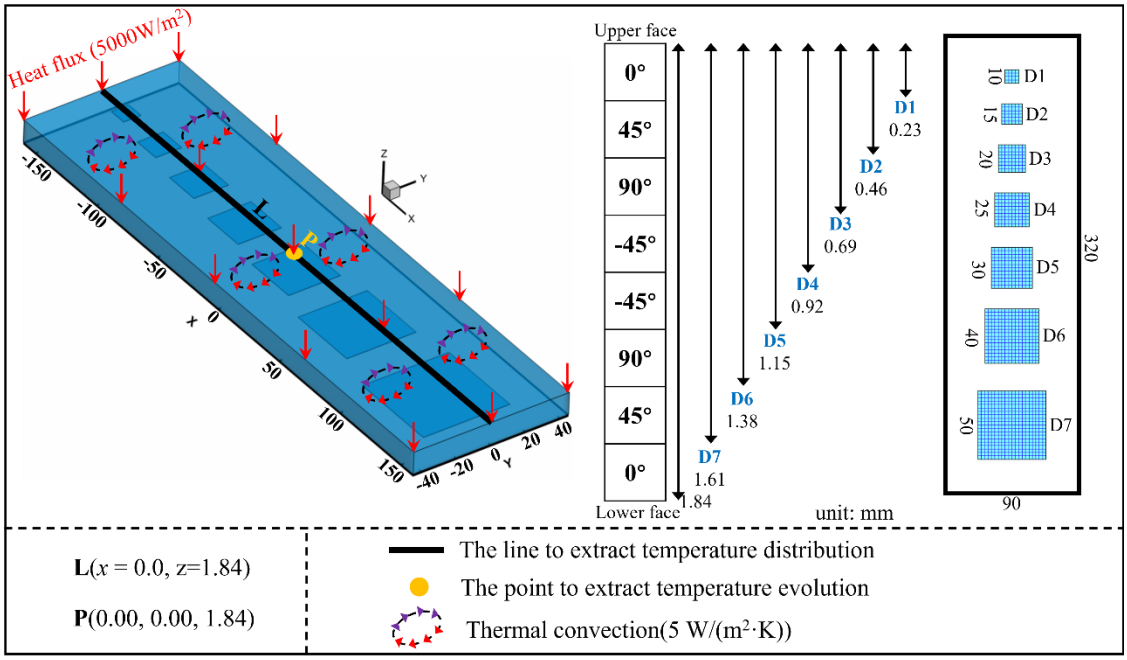


364

365 Figure 7 Numerical model of benchmark II

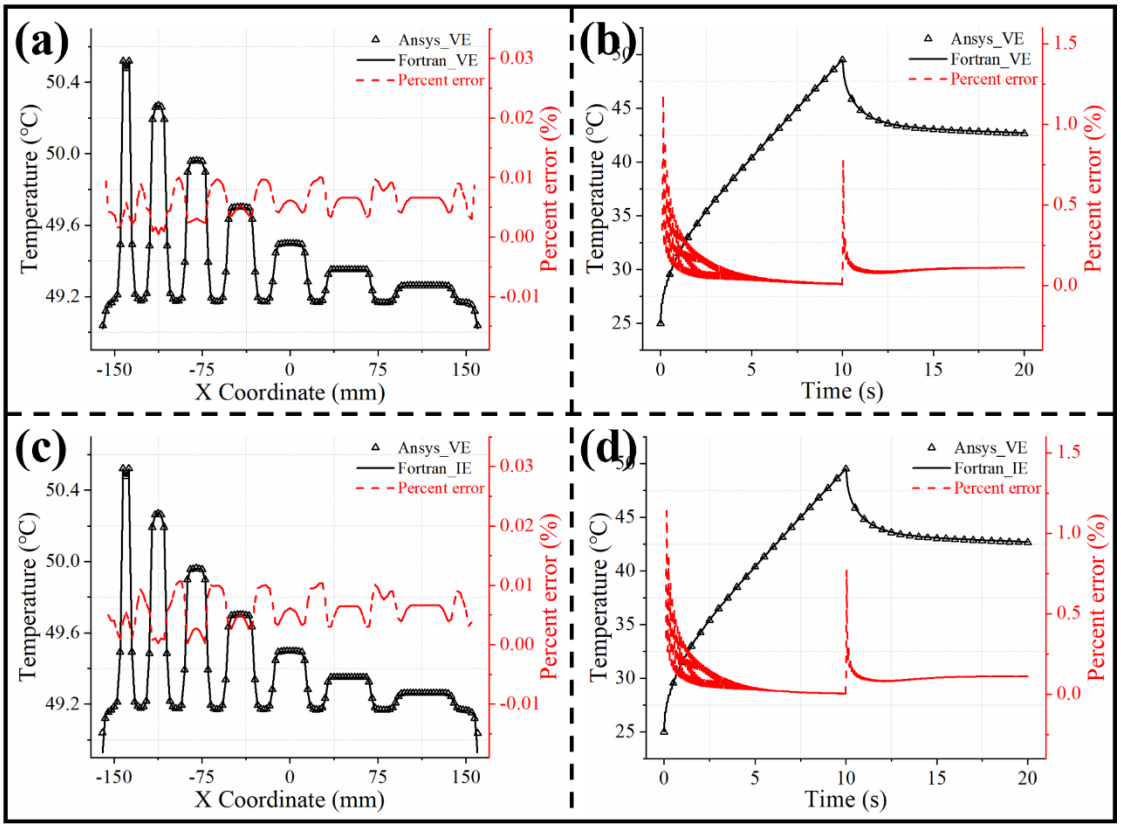


366

Figure 8 Thermal results of benchmark II comparing the classical VE method and the proposed IE method: (left) along line segment L at t = 10 s and (right) at point P.

Table 3 Simulation efficiency comparison in benchmark II

| | **Volume element VE** | **Interface element IE** |
|---|---|---|
| Number of mesh elements | 115200 | 115200 |
| Computational time (Ansys) | 31 min 32s | — |
| Computational time (Fortran) | 10min 40s | 11min 27s |

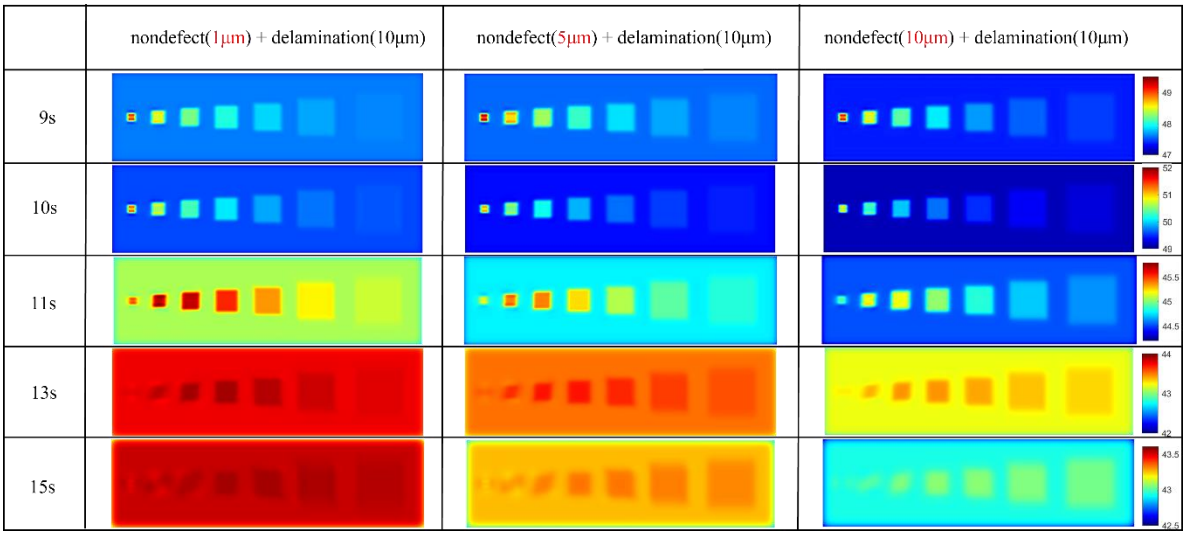


Figure 9 Surface temperature field at various time instances for different thicknesses of the sound region of the interlayer: (left) thickness = 1 μm, (middle) thickness = 5 μm, and (right) thickness = 10 μm.

## 4. PARAMETRIZED NUMERICAL METHOD

Apart from a validated and proper numerical method, it is also required to parametrize it in an efficient manner that it can provide a realistic and diverse virtual training dataset for deep learning applications. In this regard, it is crucial to account for the variable thickness and size of delaminations, to model the non-uniform and stochastic nature of heat excitation

in experiments, to consider experimental noise conditions and to diversify in the morphology of the defects.

### 4.1. Variable thickness of delamination

In section 3.1, the thickness of delamination was fixed at 10 μm, which was beneficial for the numerical validation but unrealistic in practical application. In order to investigate the effect of the delamination thickness on the thermal response, benchmark I with IE is adopted in this section. The delamination thickness ranges from 1 μm to 10 μm, while the thickness of the sound region in the interlayer equals 1 μm. The temperature distributions along the line segment L (see Fig. 3) at 10 s for different delamination thicknesses are presented in Fig. 10. Finally, the surface temperature field is presented in Fig. 11 for different time instances. As could have been expected, the delamination thickness has a significant impact on the thermal response, and as such is an essential variable when generating a virtual database for CV applications. In terms of computational efficiency, the IE approach is very interesting as it only needs to construct the global conductivity interface matrix in Eq. (22) once because the models with different delamination thicknesses have identical geometrical size. In case of VE, each delamination thickness leads to a model with a different geometrical size requiring the global conductivity matrix and global capacitance matrix in Eq. (12) to be computed repeatedly.

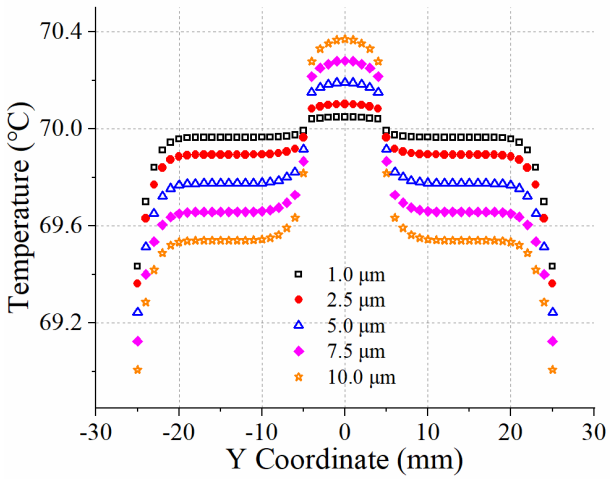


Figure 10 Temperature distribution along line segment L (see Fig. 3) for a model having a delamination with various thickness. Note that the thickness of the sound region in the interlayer is 1 μm for all cases.

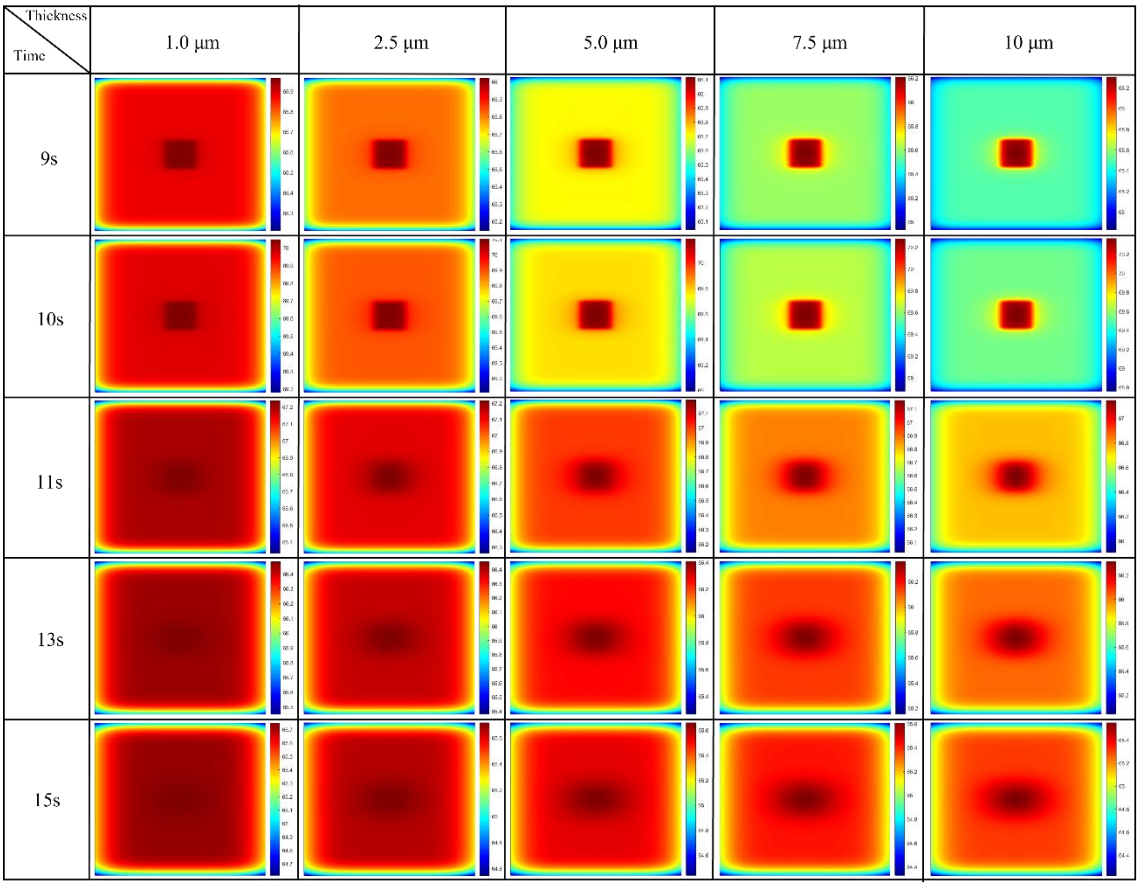


Figure 11 Surface temperature field (Benchmark I) at various time instances for different thicknesses of the delamination defect.

406

407 **4.2. Non-uniform heat excitation**

408 Following the discussion in section 2.1, the function $g(x,y)$ in equation (1) describes the
409 spatial distribution of the optical lamp at a certain distance. In case of a uniform heating
410 profile, this function can be set to 1. However, realistic optical lamps rather induce a non-
411 uniform heating profile (see Fig. 12). Therefore, the spatial distribution $g(x,y)$ has been
412 experimentally measured for typical optical lamps used in thermographic inspection, and it
413 was found that it can be described well by a 2D Gaussian distribution,

414
$$g(x,y) = \frac{p}{2\pi\sigma_X'\sigma_Y'\sqrt{1-\rho^2}} \cdot \exp\left(-\frac{1}{2(1-\rho^2)}\left[\left(\frac{X'\cos(\alpha)}{\sigma_X'}\right)^2 + \left(\frac{Y'\cos(\beta)}{\sigma_Y'}\right)^2 - 2\rho\frac{X'\cos(\alpha)\cdot Y'\cos(\beta)}{\sigma_X'\sigma_Y'}\right]\right) \quad (27)$$

415 where $p$ indicates the percentage of the lamp's energy which is effectively emitted towards
416 the sample's surface, and in our case $p$ = 0.25. $\rho$ is a correlation coefficient which is set to
417 zero, indicating that the distribution of the thermal flux does not rotate around the Z-axis.
418 Thus, Eq. (27) can be simplified to,

419
$$g(x,y) = \frac{p}{2\pi\sigma_X'\sigma_Y'} \cdot exp\left(-\frac{1}{2}\left[\left(\frac{X'\cos(\alpha)}{\sigma_X'}\right)^2\right] + \left(\frac{Y'\cos(\beta)}{\sigma_Y'}\right)^2\right) \quad (28)$$

420 where $\alpha$ and $\beta$ [°] are the rotation angles of the lamp around the Y-axis and X-axis,
421 respectively. $\sigma_X'$, $\sigma_Y'$, $X'$, and $Y'$ can be expressed as,

422
$$\sigma_X' = \sigma_X \cdot \frac{h'}{h} \quad (29)$$

423
$$\sigma_Y' = \sigma_Y \cdot \frac{h'}{h} \quad (30)$$

$$X' = x - X_{center} \tag{31}$$

$$Y' = y - Y_{center} \tag{32}$$

where $\sigma_X$ and $\sigma_Y$ [m] are experimentally derived standard deviation of the non-uniform field in x-direction and y-direction, respectively. $h$ [m] is the vertical distance between the lamp and the center of the hotspot in the experiment. $x$ and $y$ [m] are the coordinates of the point on the sample surface. $X_{center}$ and $Y_{center}$ [m] correspond to the center location of the radiated hotspot on the sample's surface. $h'$ [m] is the recalculated vertical distance between the lamp and the point on the sample, which takes rotations around x and y into account (i.e. when the lamp is not directed perpendicular to the sample) and can be written as,

$$h' = D - X' \cdot \sin\alpha - Y' \cdot \sin\beta \tag{33}$$

where D is the distance between lamp and the hotspot center in an experiment (see Fig. 12).

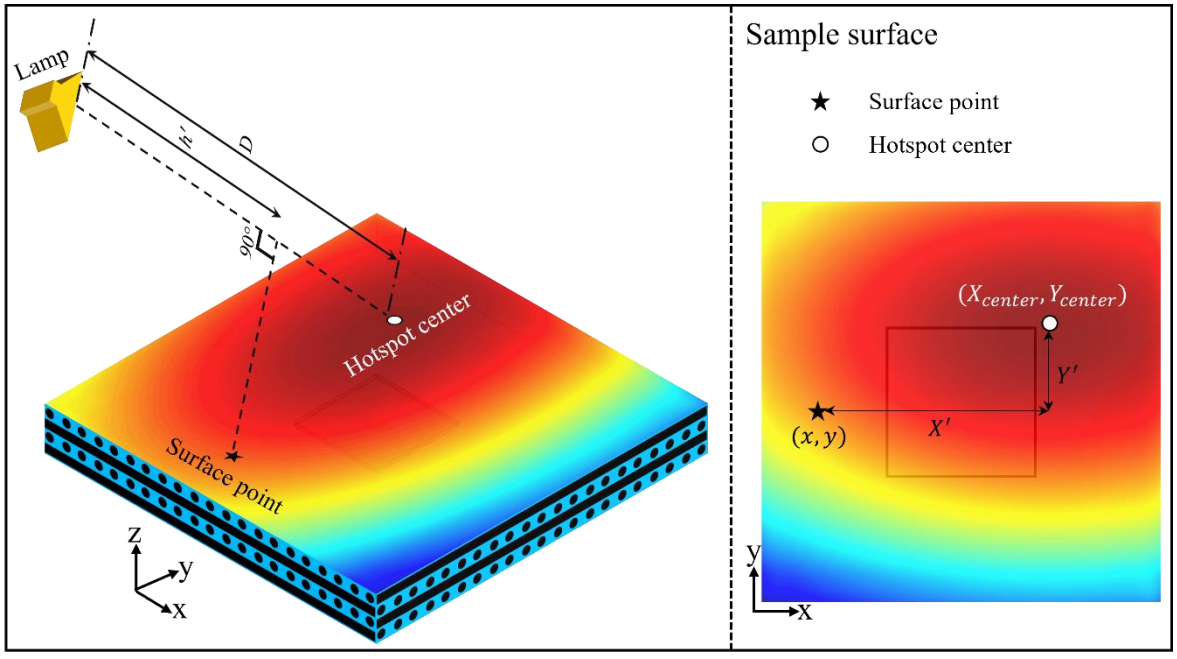


Figure 12 Schematic of the spatial distribution of a realistic optical lamp exciting the inspection surface.

For a distance $h$ = 400 mm between the employed optical lamp (Hensel linear flash lamp in our case) and the measurement plane, a fit procedure was performed for the experimentally recorded heat profile. This resulted in standard deviations $\sigma_X$ and $\sigma_Y$ of 180 mm and 100 mm, respectively. Note that the standard deviations for different distances $h$ can be easily obtained in a similar manner, from which the non-uniform heat flux can be calculated through Eq. (29) and Eq. (30). Upon running a FE model with such a non-uniform heat flux, the orientation as well as the center location of the heat flux is randomly chosen from a normal distribution. As such, this represents the randomness in how different persons position the optical excitation lamps with respect to the sample of interest during experiments. Obviously, if another excitation lamp would be used in experiment, it is necessary to know (or measure) its radiation profile and update the input parameters in the simulation model accordingly.

### 4.3. Random defect generation

Modern deep learning-based CV algorithms and image segmentation methods require sufficient diversity in their training database to achieve good prediction accuracy and generalization capability. Manually designed defect generation strategy is tedious and inefficient. Accordingly, a parametric defect generation strategy is proposed here to generate polygons with random shape (see Fig. 13). Firstly, a square base region is assigned in which defects will be generated. Then, the base region is equally divided to a number of sectors based on the polygon type. The vertices of the polygon are randomly generated in each sector. Finally, the vertices in adjacent sectors are connected. The randomly generated polygon represents the geometry of the defect. In reality, a delamination defect could have a range of

imperfect thermal contact conditions depending on its closure state. In order to cope with this scenario, the proposed FE framework randomly choses an effective thickness for the delamination area in a predefined range of 1 μm-20 μm.

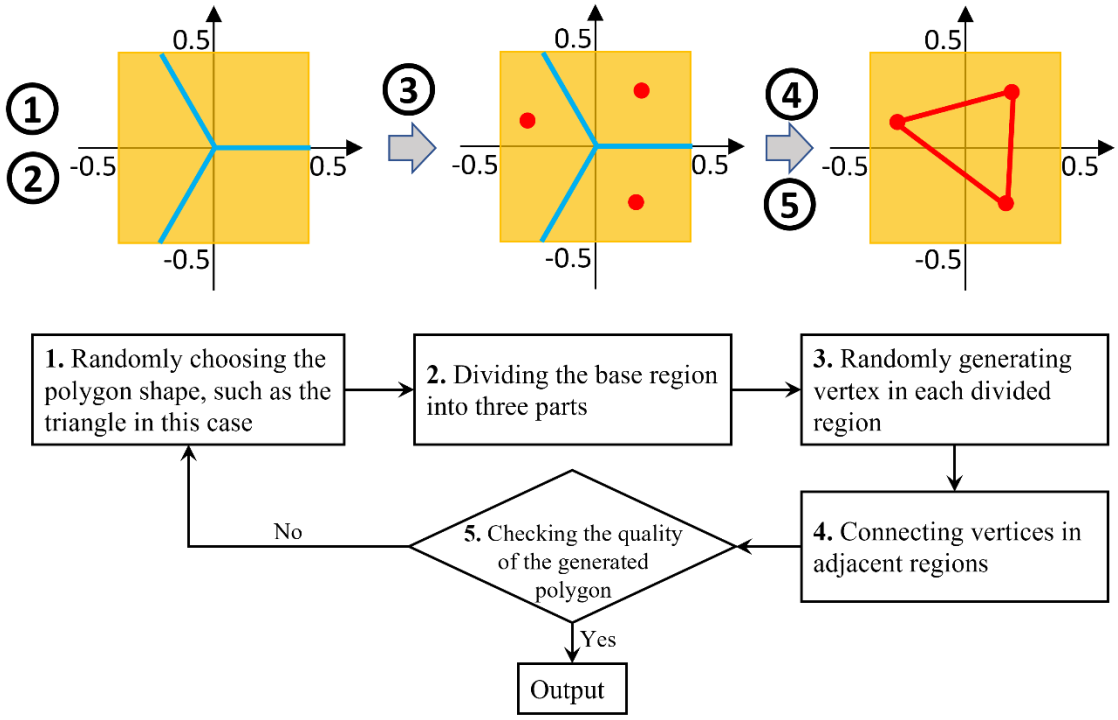


Figure 13 Stochastic defect generation process

In order to avoid the generation of polygons with extreme and unusual geometries, the algorithm accounts for five filters:

(1) The minimum area of the generated polygon should be larger than 5% of the assigned defect region.

(2) Three adjacent vertices cannot be collinear.

(3) Two adjacent vertices cannot form an angle outside the range of $20° - 160°$.

(4) Two adjacent vertices cannot be located at a distance closer than 0.1 mm from each other.

(5) The minimum distance between each vertex and the midpoint of the base region should be larger than 0.1 mm.

Obviously, this set of filters can be adapted according to the needs of the application case.

The generated polygons with random shapes are then mapped to the numerical model, whose meshes are shown in Fig. 14 for a few selected polygons. In the developed simulator, the hexahedron element shape is adopted for meshing, which leads to rough edges of the defect region. However, this effect can be alleviated through the use of smaller elements, or by considering other element shapes. The use of IE method is highly suited for calculating the thermal response for a wide set of defect geometries, sizes, thickness and depths. In contrast to the VE method, the proposed IE method employs the same mesh distribution for any randomly generated defect scenario. The global matrices are constructed once, and it is only the interface matrices that vary case by case to incorporate the defect region in the model. As such, the IE method is computationally very efficient for the generation of large thermographic databases.

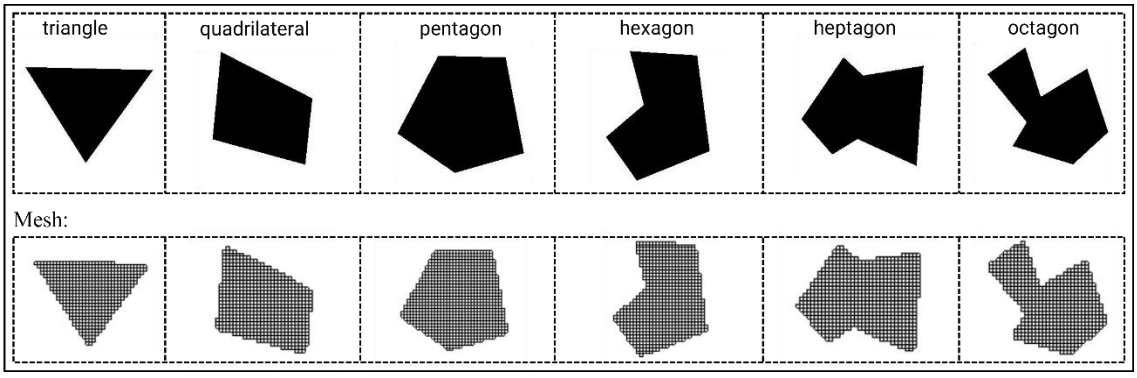


Figure 14 Random generation of defects and their discretized version.

### 4.4. Temporal noise addition

Experimental inspection conditions induce not only non-uniform heating profiles, but also temporal noise features. In order to capture this, an IRT experiment on a CFRP sample was conducted without applying an optical stimulation. The power of the temperature evolution at a single pixel can be expressed as [40],

$$logP = k - \beta logf \tag{34}$$

where $P$ is power [W], $f$ is frequency [Hz], $k$ and $\beta$ are the intercept and the slope of the regression line, respectively. Exponentiating both sides yields:

$$P = \frac{K}{f^{\beta}} \tag{35}$$

where $K$ equals $e^{k}$. The power is proportional to $1/f^{\beta}$, which can be used to characterize different noise behavior. When $\beta = 0$, power is constant at all frequencies, resulting in white noise. A value $\beta = 2$ results in red noise (or Brownian noise). When $\beta$ has a value between 0 and 2, the noise spectrum corresponds to pink noise.

Linear regression was performed on the temperature evolutions at eight random pixels in view of extracting temporal noise features. The average fitted $\beta$ equals 0.73 in the useful frequency range of 0.01-1 Hz for thermographic inspection of polymer-based materials (see figure 15 for a representative pixel). For frequencies higher than 1 Hz, the noise spectrum flattens and converges to white noise, i.e. $\beta = 0$. Therefore, pink noise with $\beta = 0.73$ and standard deviation of 15 mK, in the frequency band of 0.01-1 Hz, is added to the simulation result. This level of noise roughly corresponds to the noise equivalent temperature difference of current state-of-the-art cooled infrared cameras. In case of uncooled micro-bolometers, the

standard deviation of the noise should be rather increased to a value in the range of 45-150 mK.

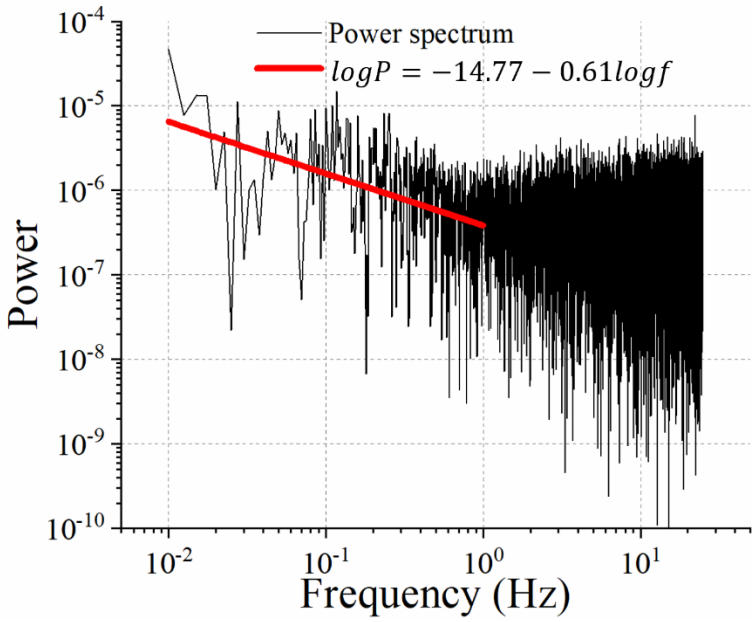


Figure 15 Power spectrum of the temperature evolution at a representative pixel and the regression line in frequency range 0.01-1 Hz.

## 5. COMPUTER VISION APPLICATION

This section investigates the feasibility to train a deep learning model with a virtual dataset from the parametrized FE framework and to achieve sufficient generalization to obtain high inference results when applying the trained classifier on experimental data. The well-documented Faster-RCNN is employed. It is a two-stage deep learning-based object detection algorithm [19], which introduces a Region Proposal Network (RPN) to embed region proposal directly in the architecture. The Faster-RCNN with a Resnet-50 backbone network was adopted in this section, which refers to the *torchvision* module in PyTorch.

The virtual training dataset consists of 1750 simulation cases, accounting for the various stochastic experimental conditions mentioned in section 4. The detailed parameters are

528 presented in table 4. Each image sequence in the virtual dataset comprises not only spatial
529 features but also temporal features. The temporal features are generally utilized to determine
530 depth information of defects, whereas spatial features are related to information on the
531 position and lateral size of defects. In this study, focus is put on defect detection and sizing
532 by using spatial features. The entire image sequence of each case cannot be fed to the Faster-
533 RCNN framework directly due to computational issues, while an individual frame cannot
534 represent all the features of the image sequence. Therefore, the data sequence has been
535 processed by TSR to achieve large data compression as well as to enhance spatial features of
536 the IRT image sequence. A fifth-degree polynomial is fit to the temperature evolution profile
537 for each pixel, and the resulting six coefficient images were utilized. Eventually, the virtual
538 training dataset comprises 10500 images, of which 90% are used for training the Faster-
539 RCNN, and 10% are used for validating the trained Faster-RCNN. The Faster-RCNN was
540 trained on the virtual dataset for 100 epochs on NVIDIA RTX 6000, while the batch size is
541 set at 12. The stochastic gradient descent (SGD) with a momentum term set to 0.9 was used
542 in Faster-RCNN, whose initial learning rate is set at 0.005. The mean average precision (mAP)
543 of Faster-RCNN in the validation dataset reaches 88.7% after 100 epochs.

544 For the testing data, flash IRT experiments were conducted on two FRP samples with
545 delamination-like defects at different depths. The flash IRT experiment was implemented
546 using the set-up in Fig. 15(a). A Hensel linear flash lamp generates a short optical excitation
547 of 5 ms with an energy of 6 kJ. The cooling stage was recorded for 20 s at a sampling
548 frequency of 30 Hz with a cooled FLIR A6750sc infrared camera in reflection mode. The
549 inspected samples are a 12-ply $[(0/90)_3]_s$ CFRP laminate of size $300 \times 300 \times 3$ mm$^3$ and a
550 8-ply $[(0/90)_2]_s$ GFRP laminate of size $300 \times 300 \times 3$ mm$^3$, both manufactured by the resin

551 transfer molding procedure. A set of delamination-like defects are introduced by means of a
552 double-folded brass foil encapsulated with flash breaker tape. At the resin injection point in
553 the middle of plates, an additional unintended defect was introduced due to the manufacturing
554 process. A schematic presentation of the two samples is displayed in Fig. 15(b-c), together
555 with an indication of the defect parameters (location, size and depth). Note that the samples
556 have been blackened before testing in order to improve the absorption of optical energy at
557 the surface.

558 The highest-order TSR coefficient images of the IRT image sequences were adopted to
559 test the Faster-RCNN which was trained on the virtual dataset. As can be seen in the selected
560 TSR images (Fig. 16(a, c)), it is not trivial to pinpoint the defects due to the irregular contrast
561 values at the defects, and the presence of a non-uniform background. Nonetheless, the
562 inference results presented in Fig. 16(b, d) show the high performance of the trained Faster-
563 RCNN in detecting the delamination-like defects. This indicates the high generalization of
564 the virtually trained Faster-RCNN owing to the highly diverse and true-to-nature database
565 generated by the parametrized FE framework. It may be expected that the proposed FE
566 framework may also be used for training more advanced deep learning models in view of
567 more challenging tasks, e.g. sizing and depth estimation of defects.
568

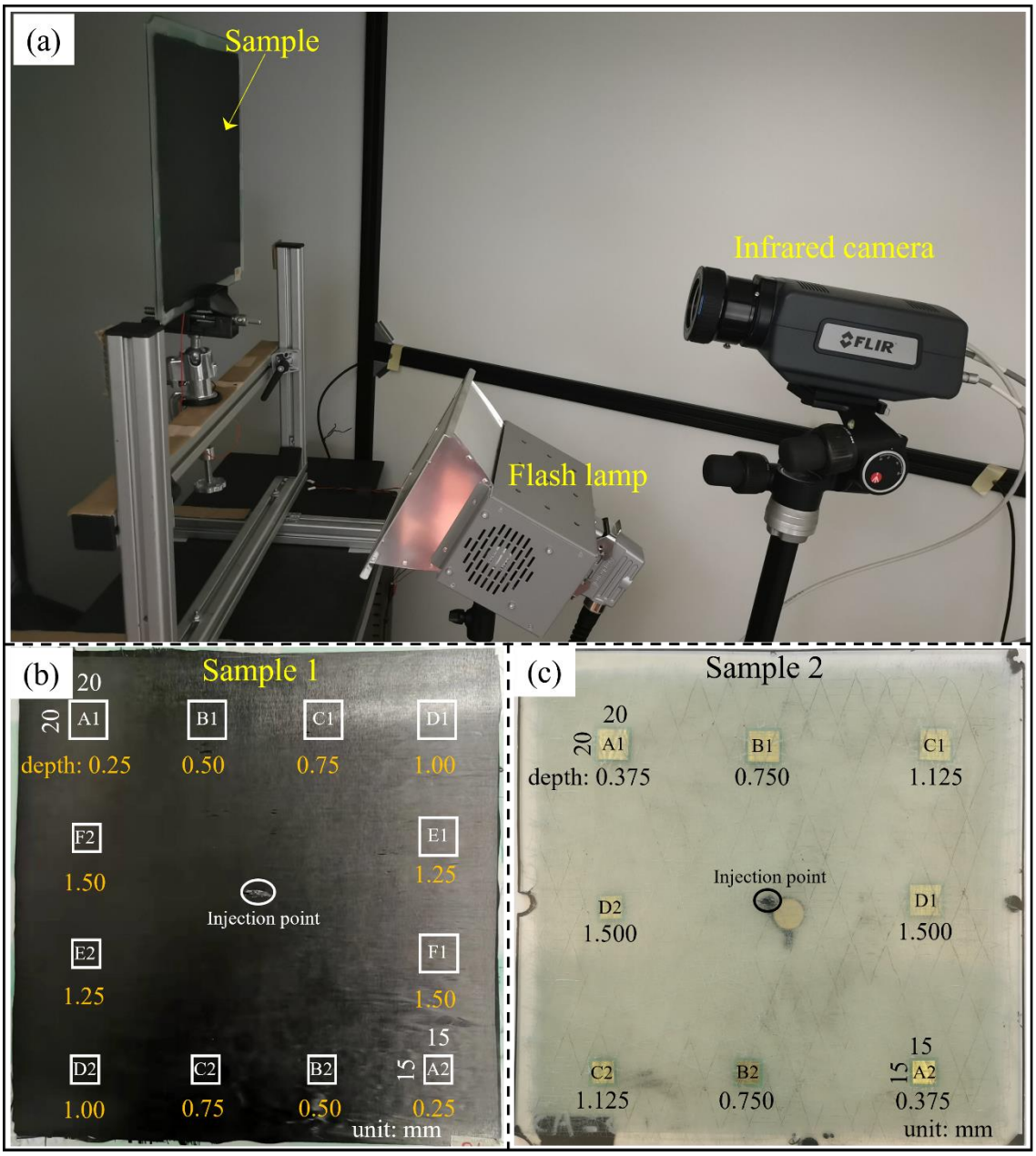


Figure 16 (a) The experimental setup, (b) CFRP sample, and (c) GFRP sample

Table 4 The parameters for dataset generation

| **Parameters** | **Values** |
|---|---|

| | |
|---|---|
| The center of the hotspot | Randomly located on the model surface |
| Defect generation area [mm$^2$] | 10×10 – 50×50 |
| Thickness of defect [μm] | 1 – 10 |
| The vertices of the polygon | 3 – 8 |
| Noise level | $\beta = 0.73$ with standard deviation of 15 mK |

573

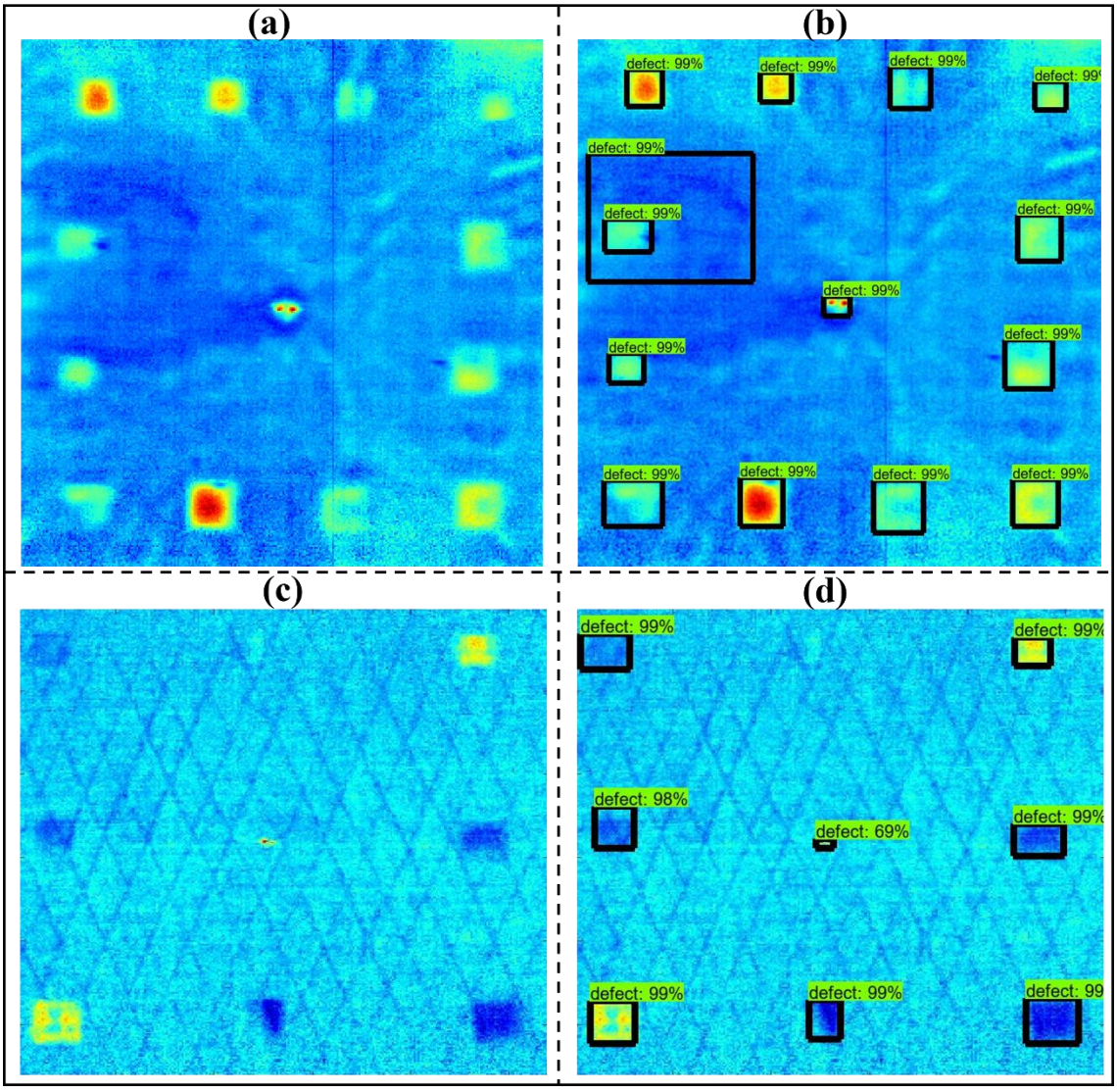


574

Figure 17 Experimental results on FRP samples with delamination-like defects: (a) TSR coefficient image and (b) inference result of CFRP sample ; (c) TSR coefficient image and (d) inference result of GFRP sample.

## 6. CONCLUSIONS AND DISCUSSIONS

A 3D FE framework is presented for optical infrared thermographic inspection of multi-layer anisotropic materials, such as fiber reinforced polymers. As an alternative to volume elements, an interface element approach is adopted for modeling of delamination-like defects. Two numerical benchmark cases have been analyzed and compared with the results from a commercial FE solver. It was found that the presented FE framework employing interface elements yields quasi-identical computation results, in both time and spatial domain, compared to the commercial FE solver using traditional volume elements. The mean error rates are well below 1%. The results show that the use of interface elements is from geometrical point-of-view more reasonable than the use of volume element for simulating delamination-like defects. In comparison with the discontinued nodes method, it is shown that the interface element approach is physically more reasonable.

The FE framework with interface element has been implemented in a parametric manner in view of efficiently generating large and diverse training datasets for computer vision applications. To obtain a high-fidelity virtual database, the typical non-uniform spatial heating profile of actual optical lamps is adopted, while realistic defect geometries are generated by means of a stochastic morphological approach employing polygons. Variable delamination thicknesses can be computed in a computationally efficient manner by means

of the interface element formulation. Temporal pink noise is added to the virtual dataset in order to further increase the diversity of the dataset. Finally, a virtual dataset was constructed using the proposed parametrized FE method, and is utilized to train the Faster-RCNN framework. The inference results on experimental data indicate that the established virtual dataset has significant potential for dense recognition tasks, like object detection and image segmentation. Several large and diverse thermographic databases will be put available to the community for use in the CV applications.

Although the proposed 3D FE framework can simulate the delamination in a geometrically rational and physically reasonable manner, the interface elements located on the sound region can be avoided using the discontinuous Galerkin method in the future since it uses completely discontinuous approximations. In addition, multiple defects can be considered in the numerical model to increase the diversity of the virtual dataset further due to that the lateral diffusion of multiple defects is much more complex. Finally, the temporal response of the IRT image sequence can be utilized to estimate defect depth.

## ACKNOWLEDGMENT

Zongfei Tong acknowledges the financial support from China Scholarship Council (CSC, grant number 202006280481) and from Bijzonder OnderzoeksFonds (BOF) of Ghent University under grant number 01N01719. Saeid Hedayatrasa acknowledges funding from Bijzonder OnderzoeksFonds (BOF) of Ghent University under grant number BOF21/PDO/041.

# REFERENCES


[1] E.J. Barbero, Introduction to composite materials design, CRC press, 2010.

[2] R. Talreja, C.V. Singh, Damage and failure of composite materials, Cambridge University Press, 2012.

[3] R. Smith, Composite defects and their detection, Materials science and engineering, 3 (2009) 103-143.

[4] R. Bossi, V. Giurgiutiu, Nondestructive testing of damage in aerospace composites, in: Polymer composites in the aerospace industry, Elsevier, 2015, pp. 413-448.

[5] M. Kersemans, I. De Baere, J. Degrieck, K. Van Den Abeele, L. Pyl, F. Zastavnik, H. Sol, W. Van Paepegem, Nondestructive damage assessment in fiber reinforced composites with the pulsed ultrasonic polar scan, Polymer Testing, 34 (2014) 85-96.

[6] J. Segers, S. Hedayatrasa, E. Verboven, G. Poelman, W. Van Paepegem, M. Kersemans, In-plane local defect resonances for efficient vibrothermography of impacted carbon fiber-reinforced polymers (CFRP), NDT & E International, 102 (2019) 218-225.

[7] R. Yang, Y. He, Optically and non-optically excited thermography for composites: A review, Infrared Physics & Technology, 75 (2016) 26-50.

[8] S. Hedayatrasa, G. Poelman, J. Segers, W. Van Paepegem, M. Kersemans, Novel discrete frequency-phase modulated excitation waveform for enhanced depth resolvability of thermal wave radar, Mechanical Systems and Signal Processing, 132 (2019) 512-522.

[9] N. Rajic, Principal component thermography for flaw contrast enhancement and flaw depth characterisation in composite structures, Composite structures, 58 (2002) 521-528.

[10] D.L. Balageas, J.-M. Roche, F.-H. Leroy, W.-M. Liu, A.M. Gorbach, The thermographic signal reconstruction method: a powerful tool for the enhancement of transient thermographic images, Biocybernetics and biomedical engineering, 35 (2015) 1-9.

[11] X. Maldague, S. Marinetti, Pulse phase infrared thermography, Journal of applied physics, 79 (1996) 2694-2698.

[12] Y. Chung, S. Lee, W. Kim, Latest Advances in Common Signal Processing of Pulsed Thermography for Enhanced Detectability: A Review, Applied Sciences, 11 (2021) 12168.

[13] F. Wang, J. Liu, P. Song, J. Gong, W. Peng, G. Liu, M. Chen, Y. Wang, Multimodal optical excitation pulsed thermography: Enhanced recognize debonding defects of the solid propellant rocket motor cladding layer, Mechanical Systems and Signal Processing, 163 (2022) 108164.
[14] G. Poelman, S. Hedayatrasa, W.V. Paepegem, M. Kersemans, Enhanced thermographic inspection of woven fabric composites by k-space filtering, Composites Part B, IN PRESS (2023).
[15] Y. He, B. Deng, H. Wang, L. Cheng, K. Zhou, S. Cai, F. Ciampa, Infrared machine vision and infrared thermography with deep learning: a review, Infrared Physics & Technology, (2021) 103754.
[16] R. Marani, D. Palumbo, U. Galietti, T. D'Orazio, Deep learning for defect characterization in composite laminates inspected by step-heating thermography, Optics and Lasers in Engineering, 145 (2021) 106679.
[17] P. Kovács, B. Lehner, G. Thummerer, G. Mayr, P. Burgholzer, M. Huemer, Deep learning approaches for thermographic imaging, Journal of Applied Physics, 128 (2020) 155103.
[18] L. Cheng, Z. Tong, S. Xie, M. Kersemans, IRT-GAN: A generative adversarial network with a multi-headed fusion strategy for automated defect detection in composites using infrared thermography, Composite Structures, (2022) 115543.
[19] S. Ren, K. He, R. Girshick, J. Sun, Faster R-CNN: Towards Real-Time Object Detection with Region Proposal Networks, Ieee Transactions on Pattern Analysis and Machine Intelligence, 39 (2017) 1137-1149.
[20] J. Redmon, A. Farhadi, Yolov3: An incremental improvement, arXiv preprint arXiv:1804.02767, (2018).
[21] O. Ronneberger, P. Fischer, T. Brox, U-Net: Convolutional Networks for Biomedical Image Segmentation, in: N. Navab, J. Hornegger, W.M. Wells, A.F. Frangi (Eds.) Medical Image Computing and Computer-Assisted Intervention, Pt Iii, 2015, pp. 234-241.
[22] L.-C. Chen, G. Papandreou, F. Schroff, H. Adam, Rethinking atrous convolution for semantic image segmentation, arXiv preprint arXiv:1706.05587, (2017).

[23] Q. Fang, C. Ibarra-Castanedo, X. Maldague, Automatic defects segmentation and identification by deep learning algorithm with pulsed thermography: Synthetic and experimental data, Big Data and Cognitive Computing, 5 (2021) 9.
[24] T. Chu, A. Mahajan, A. DiGregorio, S. Russell, Determination of optimal experimental parameters for transient thermography imaging using finite-element models, The Imaging Science Journal, 53 (2005) 20-26.
[25] F. Lopez, V. de Paulo Nicolau, C. Ibarra-Castanedo, X. Maldague, Thermal–numerical model and computational simulation of pulsed thermography inspection of carbon fiber-reinforced composites, International Journal of Thermal Sciences, 86 (2014) 325-340.
[26] A. Ratsakou, C. Reboud, A. Skarlatos, D. Lesselier, Fast simulation approach dedicated to infrared thermographic inspection of delaminated planar pieces, in: AIP Conference Proceedings, AIP Publishing LLC, 2019, pp. 120004.
[27] M. Krishnapillai, R. Jones, I.H. Marshall, M. Bannister, N. Rajic, NDTE using pulse thermography: Numerical modeling of composite subsurface defects, Composite Structures, 75 (2006) 241-249.
[28] Q. Yi, G. Tian, H. Malekmohammadi, S. Laureti, M. Ricci, S. Gao, Inverse reconstruction of fibre orientation in multilayer CFRP using forward FEM and eddy current pulsed thermography, NDT & E International, 122 (2021) 102474.
[29] M. Susa, C. Ibarra-Castanedo, X. Maldague, A. Bendada, S. Svaic, I. Boras, Pulse thermography applied on a complex structure sample: comparison and analysis of numerical and experimental results, in: IV Pan American Conference for Non Destructive Testing, 2007.
[30] H. Liu, C. Pei, S. Xie, Y. Li, Y. Zhao, Z. Chen, Inversion Technique for Quantitative Infrared Thermography Evaluation of Delamination Defects in Multilayered Structures, Ieee Transactions on Industrial Informatics, 16 (2020) 4592-4602.
[31] Standard test method for mode I interlaminar fracture toughness of unidirectional fiber-reinforced polymer matrix composites, ASTM Internat., 2007.
[32] C. Maierhofer, M. Röllig, M. Gower, M. Lodeiro, G. Baker, C. Monte, A. Adibekyan, B. Gutschwager, L. Knazowicka, A. Blahut, Evaluation of different techniques of active thermography for quantification of artificial defects in fiber-reinforced composites using

thermal and phase contrast data analysis, International Journal of Thermophysics, 39 (2018) 1-37.
[33] R. de Borst, Chapter 4 - Interface Elements, in: R. de Borst (Ed.) Computational Methods for Fracture in Porous Media, Elsevier, 2018, pp. 47-67.
[34] G.E. Blandford, T.R. Tauchert, Thermoelastic analysis of layered structures with imperfect layer contact, Computers & Structures, 21 (1985) 1283-1291.
[35] J.A. Karjalainen, A simple method to form interface elements in the heat transfer analysis, Communications in applied numerical methods, 3 (1987) 297-300.
[36] A. Corigliano, Formulation, identification and use of interface models in the numerical analysis of composite delamination, International Journal of Solids and Structures, 30 (1993) 2779-2811.
[37] Y. Mi, M.A. Crisfield, G.A.O. Davies, H.B. Hellweg, Progressive delamination using interface elements, J Compos Mater, 32 (1998) 1246-1272.
[38] G. Poelman, S. Hedayatrasa, J. Segers, W. Van Paepegem, M. Kersemans, Adaptive spectral band integration in flash thermography: Enhanced defect detectability and quantification in composites, Composites Part B: Engineering, 202 (2020) 108305.
[39] K.-J. Bathe, Finite element procedures, Prentice Hall, 2006.
[40] A. Downey, Think DSP: digital signal processing in Python, " O'Reilly Media, Inc.", 2016.